Analysis of Dual-Frequency Ocean Backscatter Measurements at Ku- and Ka-Bands Using Near-Nadir Incidence GPM Radar Data

Frédéric Nouguier, Alexis Mouche, Nicolas Rascle, Bertrand Chapron, and Douglas Vandemark

***Abstract*—Global colocalized ocean surface measurements using the Global Precipitation Measurement near-nadir dual-frequency Ku- and Ka-band microwave measurements are analyzed and compared. Focusing on the Ka and Ku cross-sections fall-off with incidence angles, the contemporaneous measurements enable to more precisely document differing ocean scattering characteristics for both microwave frequencies. Sensitivity with wind speed and significant wave height is further reported using global comparisons with numerical estimates. As demonstrated, the bifrequency capability can provide direct means to efficiently separate short-scale wave contributions, between mean squared slope and curvature characteristics, and to further gain valuable insights concerning near-nadir instruments onboard future ocean satellite missions including the China–France Oceanography Satellite and the Surface Water Ocean Topography Mission.**

***Index Terms*—Microwave, radar cross section, scattering, spaceborne radar.**

I. Introduction

THIS letter attempts to isolate and interpret subtle but measurable wind-dependent differences between near-nadir ocean radar backscattter data observed at Ku- and Ka-bands. The interpretation involves inference of ocean surface wave slope and curvature statistics assuming quasi-specular radar reflection from the sea. This new global view of sea surface microwave scattering at short centimeter to millimeter frequencies is provided by the dual-frequency precipitation radar (DPR) onboard the Global Precipitation Measurement (GPM) mission satellite platform. With exactly matching surface antenna footprints at and around nadir incidence angles, the Ku- and Ka-band PR normalized radar cross section (σ^0) measurements enable systematic and colocalized analysis of differing ocean scattering characteristics. As shown in this letter, bifrequency data analysis appears to provide a means to separate surface slope and curvature effects. This can lead to a refined estimation of the fine-scale sea surface roughness at the centimeter scale that is, in turn, related to physical air–sea processes such as the local wind stress and the rate of gas exchange across the sea surface.

The present study builds on previous satellite observations where the new DPR data now combine dual frequency and incidence angle diversity that were before separated. For example, dual-frequency altimeter (nadir only) σ^0 observations and analyses used global sampling obtained using TOPEX [1], [2], at both C- and Ku-bands along with significant wave height (SWH) estimates, to suggest an approach that better isolates short-scale wind wave information and can lead to improved wind speed estimates (e.g., [3]–[5]). As understood, if very short scale roughness elements were not present, wind-dependent returns at both frequencies would be identical. However, clear wind dependence is systematically observed for the ratio σ^0_C/σ^0_{Ku}. Analyses of this C-Ku combination [1], [2] point out that the critical surface wavelength scales of interest must lie in the short gravity-capillary wave range.

Additional near-nadir data have been provided by the large TRMM KuPR dataset. Using TRMM, it is possible to use spaceborne rain radar data to obtain Ku-band microwave ocean surface σ^0 measurements across a small but important range of near-nadir incidence angles [6]. The added angular information provides a more complete analysis under the quasi-specular scattering framework. Moreover, [7] colocalized satellite altimeter-derived SWH with TRMM data to document the impacts of both wind speed (short wave) and longer scale gravity waves on σ^0 and its variation with incidence angle. Chu *et al.* [8], [9] then extended this analysis to study asymmetry and anisotropy of the Ku-band near-nadir backscatter signals.

Now, the DPR onboard GPM provides systematic colocalized Ka- and Ku-band measurements, leading to large and statistically meaningful data sets, and data covering the same range of incidence angles $(0^\circ - 9^\circ)$ provided by TRMM. To exploit both bifrequency and incidence angle aspects of the GPM DPR, we propose to use a method similar to [10] and [11] that relies foremost on the analysis of σ^0 incidence fall-off to derive sea surface parameters. This relaxes the need to have precisely intercalibrated Ku- and Ka-band measurements and, for instance, the known differing SST impact on Ka- and Ku-band Fresnel coefficients (e.g., [12]).

Section II presents an overview of the Ku- and Ka-band σ^0 measurements and global comparisons with numerical wind and wave parameter estimates. Section III uses an extended physical optics (PO) scattering approach to develop an interpretation of GPM σ^0 fall-off sensitivity at both frequencies that

Manuscript received December 29, 2015; revised April 18, 2016 and June 10, 2016; accepted June 20, 2016. Date of publication July 11, 2016; date of current version August 5, 2016.

F. Nouguier is with the Mediterranean Institute of Oceanography, 13288 Marseille, France, and also with the Université de Toulon, CNRS/INSU, IRD, 83957 La Garde, France (e-mail: frederic.nouguier@gmail.com).

A. Mouche, N. Rascle, and B. Chapron are with the Laboratoire d'Océanographie Spatiale, Ifremer, 29280 Plouzané, France.

D. Vandemark is with the Institute for the Study of Earth, Oceans, and Space, University of New Hampshire, Durham, NH 03824 USA.

Color versions of one or more of the figures in this paper are available online at http://ieeexplore.ieee.org.

Digital Object Identifier 10.1109/LGRS.2016.2583198

includes relating these high-frequency microwave observations to the well-known Cox and Munk measurements [13]. We then demonstrate that a bifrequency analysis can be used to separate long- and short-scale roughness element impacts on GPM σ^0, with the new result being the capability to better infer total sea surface mean squared slope and the influence of small-scale curvature.

II. GPM, An Opportunity For Ocean Remote Sensing

A. *GPM Ku and Ka DPR*

Launched on February 27, 2014, the GPM mission provides new and unexplored data over the ocean. While the GPM mission is primarily designed to provide new information on rain and snow precipitation estimates, the ocean remote sensing community can also explore this new global source of information on ocean backscatter.

The GPM platform carries the first spaceborne Ku-/Ka-band DPR and a multichannel microwave imager (GMI). In particular, the KaPR operates at 35.5 GHz with a nadir-oriented antenna. The 0.7° beamwidth antenna sweeps a 120-km swath providing a 5 km $\times$ 5 km surface footprint. The KuPR, coaligned with the KaPR, operates at 13.6 GHz and provides a wider 245-km swath but with the same 5 km $\times$ 5 km resolution. As designed, KuPR and KaPR have 25 matched beams to provide perfectly colocalized Ku/Ka measurements for incidence angles between $-9°$ and 9°.

For this study, selected data correspond to the nominal swath (NS) of the KuPR and the colocalized matched swath (MS) of the KaPR. Acquisitions over land, ice, and raining regions as well as those with flagged as poor quality were removed, leading to 165157 points for the Ku-band set and 85 729 points for the Ka-band set.

B. *Ocean Wave Model Colocation and Data Analysis*

For all selected points, the outputs of the *Wave Watch III* (WW3) ocean surface wave model were coregistered with GPM to provide surface wind speed and SWH estimates. The WW3 model output was provided with a 0.5°/1 h spatiotemporal resolution.

Fig. 1 shows the nearest-to-nadir incidence ($\theta = 0.7°$) Ka-band σ^0 versus SWH for different wind speeds. As expected, Ku- (not shown here) and Ka-band σ^0 measurements are sensitive to both wind speed and the sea state's degree of development, i.e., SWH. The latter sensitivity of σ^0 to SWH decreases with increasing wind speed and also for higher incidence angles (up to 9°, not shown), consistent with previous studies [7]–[9]. However, at a given SWH, the σ^0 changes with wind speed are found to be slightly higher at Ka- than at Ku-band. This is in line with results recently reported by [14] using SARAL-Altika and Envisat-RA altimeter measurements.

III. Physical Interpretation

A. *Adapted Scattering Model*

The geometrical optics (GO) approximation for electromagnetic (EM) scattering from rough sea surfaces is still widely

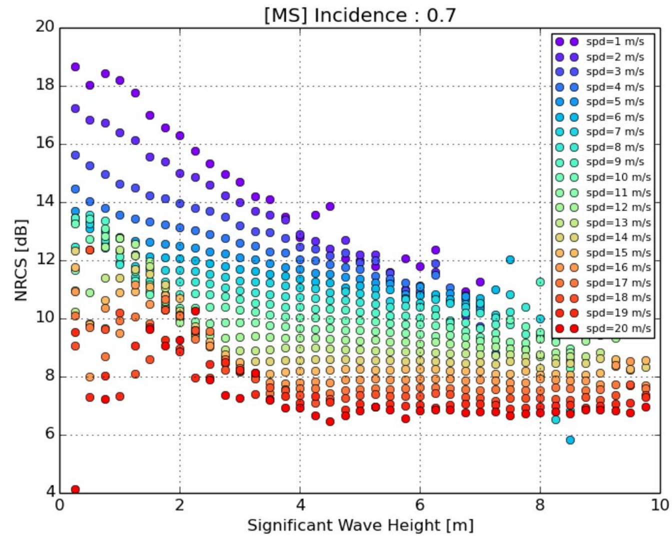

Fig. 1. KaPR σ^0 versus SWH at $\theta = 0.7°$.

used to interpret nadir and near-nadir microwave radar measurements [15]. A GO model solely relates the radar cross section to the sea surface slope probability distribution function and should thus be insensitive to the EM radar wavelength (except for the impact of seawater permittivity). For millimeter-wave (Ka-band) sensors and ocean surfaces, where the known roughness elements are longer than 5 mm or so, this optical assumption should be quite valid, effectively approaching the response of VIS sensors. Hereafter, we briefly recall the GO formulation.

Denoting $\boldsymbol{K}_0$ and $\boldsymbol{K}$ as the incident and scattered EM wave vectors and then their respective horizontal $\boldsymbol{k}_0$, $\boldsymbol{k}$ and vertical $-q_0$, q components, one has

$$\boldsymbol{K}_0 = \boldsymbol{k}_0 - q_0\hat{z}, \qquad \boldsymbol{K} = \boldsymbol{k} + q\hat{z} \tag{1}$$

with $q,\ q_0 > 0$ and $k_0^2 + q_0^2 = k^2 + q^2 = K_0^2$, and one can define the Ewald vector $\boldsymbol{Q} = \boldsymbol{K} - \boldsymbol{K}_0$ with horizontal $\boldsymbol{Q}_H = \boldsymbol{k} - \boldsymbol{k}_0$ and vertical $Q_z = q + q_0$ components. The GO approximation can then become

$$\sigma^0 = \frac{4\pi|\mathcal{K}|^2}{Q_z^4} P_{\eta'}\left(\frac{\boldsymbol{Q_H}}{Q_z}\right) \tag{2}$$

where $P_{\eta'}$ is the bidimensional slope probability density function (pdf) of the surface and $\mathcal{K}$ is the Kirchhoff kernel related to the Fresnel coefficient. $\mathcal{K}$ depends on both the incidence angle and EM frequency. Under an isotropic Gaussian assumption for the sea surface slope distribution, (2) simplifies to

$$\sigma^0 = \frac{|R|^2}{\text{mss}_T} \sec^4(\theta) \exp\left(-\frac{\tan^2(\theta)}{\text{mss}_T}\right) \tag{3}$$

where θ is the radar incidence angle, mss_T is the total mean square slope, and $|R|$ is the Fresnel coefficient at normal incidence.

This form (3) supports the popular and robust approach to use a Gaussian fit with θ to analyze σ^0 in the microwave regime. However, as generally reported, the shape of the logarithm of the near-nadir σ^0 fall-off is indeed very close to the parabolic-Gaussian approximation but with a faster fall-off compared to optical measurements. The estimate parameter, called $\text{mss}_{\text{shape}}$ hereafter, is always smaller than its optical counterpart: mss_T.

The commonly invoked physical interpretation of this discrepancy from the optical assumption is that the longer EM wavelength acts like a physical filtering/sampling of the surface roughness spectrum; in effect, shorter elements remain unseen. An alternative explanation is given in [16], where they posit that non-Gaussianity in the sea surface slope distribution could produce a similar deviation in σ^0 fall-off with θ [11].

For this study, a first-order correction to the GO model for curvature impact is next imposed based on the PO formulation (i.e., GO4 model [17]). For the isotropic case and considering the correction to be small, a Gram–Charlier development can be used and written as

$$\sigma^0 = \frac{|R|^2 \sec^4(\theta)}{\text{mss}_T} \exp\left(-\frac{\tan^2(\theta)}{\text{mss}_T}\right) \times \left[1 + \frac{\alpha}{4}\left(\frac{\tan^4(\theta)}{\text{mss}_T^2} - 4\frac{\tan^2(\theta)}{\text{mss}_T} + 2\right)\right] \quad (4)$$

where

$$\alpha = \frac{2\lambda_4}{3} + \frac{\text{msc}}{Q_z^2 \text{mss}_T^2} \quad \text{with} \quad Q_z = 2K_0 \cos(\theta) \quad (5)$$

with a correction that encompasses λ_4, a kurtosis (frequency-independent) coefficient that can be related to c_{04} and c_{40} [15, eq. (12)]). These are the fourth-order statistical parameters introduced by [13] ($\lambda_4 = c_4$). The right-hand term holds a frequency-dependent correction related to msc, a parameter directly linked to the short-scale sea surface mean squared curvature. This correction term vanishes as the EM wavelength approaches submillimeter wavelengths. Note also that the isotropic assumption cancels out the skewness coefficient introduced by [13]. To interpret this GO4 modification, if one assumes the overall statistical and geometrical correction sufficiently small (e.g., for Ka-band measurements) and also considers only shallow small incidence angles, a direct identification of the $\tan^2(\theta)$ factor in (4) leads to

$$\text{mss}_{\text{shape}} \simeq \text{mss}_T \div (1 + \alpha). \quad (6)$$

Equations (6) and (5) explain why the shape parameter is always smaller than the total mean square slope. According to (5), this difference can be attributed to both the non-Gaussian nature of the surface (kurtosis λ_4), independent of the EM wavelength, and a frequency-dependent correction due to both surface curvature and slope. Thus, as interpreted, the shape parameter does not necessarily correspond to a particular statistical parameter linked to a filtered surface and/or a precise facet-size definition. For low-surface-curvature conditions and large EM frequency, α reduces to solely a non-Gaussian surface correction. The pure tangent-plane approximation holds, and the GO model is recovered. However, if the mean squared curvature correction term increases and/or Q_z decreases, then α will increase, and the PO model departs from GO. While weak, polarization sensitivity [18] is also expected. Accordingly, the key parameter controlling GO-departure is α, and this parameter will be much larger for Ku- than for Ka-band measurements (Q_z effect). At Ku-band, the roughness correction is almost ten times larger than at Ka-band. Therefore, the simplified Gram–Charlier development (4) does not necessarily hold. However, contemporaneous Ku- and Ka-band measurements from GPM may hold information to refine characterization of the wind dependence in fine-scale wavelets present on the surface.

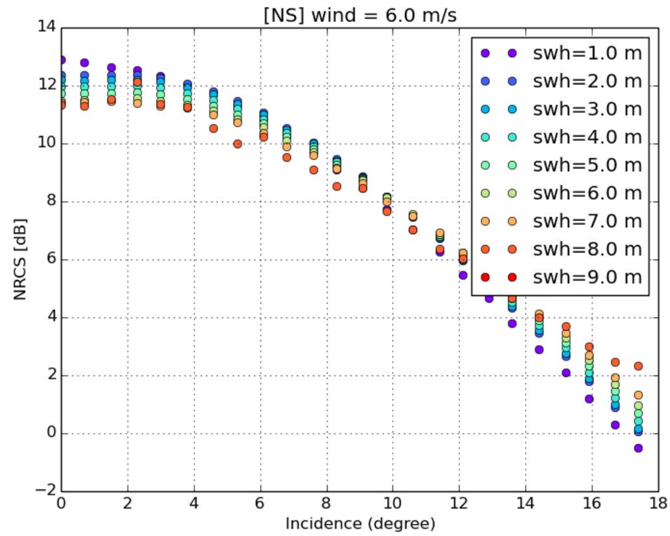

Fig. 2. KuPR σ^0 versus incidence at $U_{10} = 6\ \text{m} \cdot \text{s}^{-1}$.

B. Shape Parameter

As illustrated in Fig. 2, the σ^0 dependence with incidence angle closely follows the expected parabolic-shape assumption for both Ka- and Ku-bands and for a wide range of wind speeds ($0 < U_{10} < 18\ \text{m} \cdot \text{s}^{-1}$) and SWH ($0 < \text{SWH} < 6.5\ \text{m}$). The form of (3) appears to agree well with the observed incidence fall-off of σ^0, and so, we can invert the shape parameter $\text{mss}_{\text{shape}}$ using a linear regression in the ($\log(\cos^4(\theta)\sigma^0$, $\tan^2(\theta)$) domain (the $\text{mss}_{\text{shape}}$ corresponds to the inverse of the slope coefficient). However, deviations from the Gaussian law are most noticeable for very low sea states and/or at the largest incidence angles. In these cases, the $\text{mss}_{\text{shape}}$ parameter is the dominant term in the decrease of σ^0 with angle, and its estimate depends on the range of angles used in the regression. To avoid this artifact, the Student's t-distribution is used on data over the full range of incidence angles [16]. This distribution can account for deviations from parabolic behavior at off-nadir angles while maintaining parabolic dependence near nadir. The retrieval of the shape parameter from this regression is robust with respect to the range of incidence angles that are used.

Fig. 3 displays the resulting $\text{mss}_{\text{shape}}$ as a function of wind speed and sea state for the Ku- and Ka- bands. It clearly illustrates, for both bands, variability in the shape parameter with the SWH under low-wind-speed conditions. With increasing wind speed, shorter scale waves will start to exhibit larger slopes. Steep short-scale waves are more strongly coupled with the wind speed [19] and become the dominant contribution to

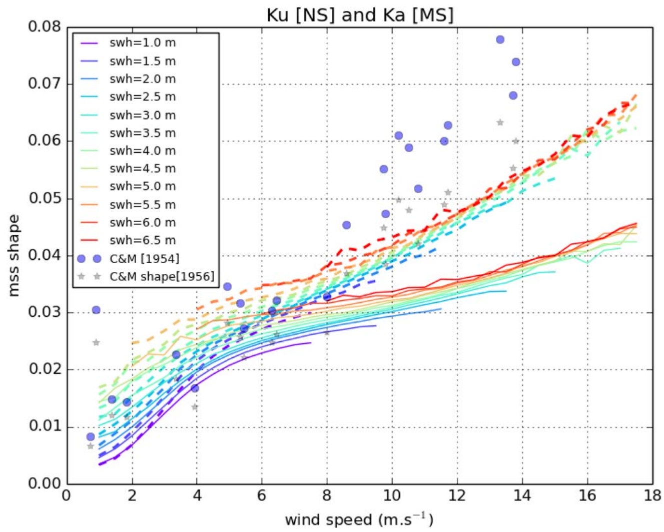

Fig. 3. Mss shape versus wind speed for different SWHs. Colored curves are derived from the regression of the Ku/Ka DPR incidence variations. Solid lines stand for the Ku-band, and dashed lines stand for the Ka-band. Blue points are C&M 54 reference points. Gray stars are C&M points without kurtosis correction, i.e., their $\mathrm{mss}_{\mathrm{shape}}$.

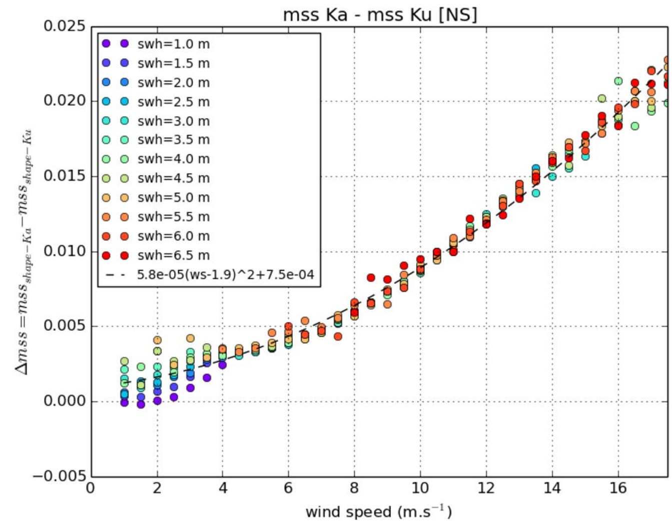

Fig. 4. Difference between Ka and Ku mss shapes.

the shape mean square slope. The result is a lower relative dependence of $\mathrm{mss}_{\mathrm{shape}}$ on SWH variation under higher wind speed conditions.

The blue points in Fig. 3 represent the so-called total mean square slope estimates. They are provided as reference estimates based on the optically based measurements reported by [13]. As discussed in [20], Cox and Munk could not directly measure the occurrence of the very infrequent steepest wave slopes with sufficient accuracy to include these important contributors to the total slope pdf. Thus, a so-called *blanket* procedure, also including the non-Gaussian contributions, was used to produce an *ad hoc* normalized pdf (see [16] for a more detailed discussion). This extra contribution is wind independent and simply involves the application of a constant (enhancement) of ~1.23. This factor relates their (measured) optical shape parameter to the (expected) total mean squared slope parameter. The gray stars in Fig. 3 thus represent the "C&M $\mathrm{mss}_{\mathrm{shape}}$," as derived from their data in the nonnormalized distribution and as obtained in the optical domain.

As for the Cox and Munk experiment, GPM bifrequency data do not cover sufficiently large incidence angles. Thus, even if one includes the PO correction term carrying the curvature effect, when one uses the smallest incidence angles [see (4)], the total mean square slope is difficult to recover using the regression of σ^0 fall-off. Accordingly, this Ku- and Ka-band $\mathrm{mss}_{\mathrm{shape}}$ is best compared to the $\mathrm{mss}_{\mathrm{shape}}$ derived from optical measurements. This most direct comparison should first help to assess the non-Gaussian correction that should be common to all measurements. As obtained, this indeed helps to better reconcile optical and high-frequency microwave data analysis. Especially at low wind speeds, scales involved in the scattering process are mostly larger than the EM wavelengths. The σ^0 fall-off is then similar for the two microwave bands as well as for the optical case. It results in very close $\mathrm{mss}_{\mathrm{shape}}$ values for the three acquisitions. Note that Cox and Munk measurements do not exhibit SWH variability. This is because their data, acquired over a coastal area, were mainly obtained under low-sea-state conditions.

For wind speeds larger than 7 m $\cdot$ s^{-1}, the $\mathrm{mss}_{\mathrm{shape}}$'s for both Ku- and Ka-bands are systematically observed to be smaller than that for optical. However, as expected, the correction related to the finite scale of the EM wavelength and the growth of short-scale roughness elements leads to a lower $\mathrm{mss}_{\mathrm{shape}}$ value for the Ku- (2.2 cm) than the Ka-band (8.4 mm) measurements.

This is further illustrated by considering the difference between $\mathrm{mss}_{\mathrm{shape}}$'s at the two frequencies

$$\Delta\mathrm{mss}_{\mathrm{shape}} = \mathrm{mss}_{\mathrm{shape\text{-}Ka}} - \mathrm{mss}_{\mathrm{shape\text{-}Ku}}. \tag{7}$$

As developed, this difference is expected to eliminate non-Gaussian impacts and is directly related to deviation from the GO approximation due to short-scale curvature effects. Fig. 4 illustrates this difference $\Delta\mathrm{mss}_{\mathrm{shape}}$ (7) against wind speed for the different SWH classes. As observed, the strong SWH dependence is now severely attenuated. Indeed, the longer waves that dominate SWH and are often dissociated from the local wind field are certainly equally resolved by the individual microwave instruments. However, this $\Delta\mathrm{mss}_{\mathrm{shape}}$ measurement efficiently cancels this long wave contribution. The remaining signal is then frequency-dependent small-scale roughness corrections. Mostly starting above a wind speed of 7 m/s, these corrections are then likely dominated by the growth in steep short surface roughness scales, possibly exhibiting high curvature near their crests [21], but also possibly due to enhanced generation of short-crested surface roughness disturbances generated by breaking waves, including parasitic capillary waves [19].

Foremost, retrieving the total mss from GPM measurements remains challenging. The mathematical approximation (4) is certainly justified for the Ka-band but likely limited for the Ku-band. The GPM incidence excursion of the Ka-band (9°) is also too small to help derive precise curvature and slope variance parameters. More quantitatively, it is the difference between mss shapes derived from optical measurements and Ka-band that can be exploited to infer an effective fourth-order (mean squared curvature) msc correction. At 10 m/s, a numerical evaluation leads to msc $\simeq 1200$, to be compared with stereophotograph estimates of sea surface curvature [22, Fig. 11] or other mathematical approaches [23, Fig. 5.12].

An additional observation is the stronger dependence of this $\Delta \mathrm{mss}_{\mathrm{shape}}$ with wind speed, where we observe a nearly quadratic dependence in comparison to the more linear dependence of mss with wind speed. Thus, the Ku- and Ka-band difference data already indicate a means to infer the variable production of rougher surface elements at short scale as winds increase. These elements will contribute to enhance the form drag; thus, this derived parameter can then become a possible robust proxy to better infer wind stress at the surface and/or the air–sea gas transfer velocity. We also expect that the high resolution of GPM bifrequency radar measurements (5 km), coupled with the concurrent SST derived with the onboard GPM passive microwave (GMI) measurements, will allow for the evaluation of surface roughness contrasts across the satellite swath to detect small-scale wave variations that result from air–sea coupling tied to strong meso- and submesoscale SST variations and surface currents (i.e., [24]).

IV. Conclusion

Global colocalized ocean surface measurements using the GPM near-nadir dual-frequency Ku- and Ka-band active microwave measurements have been analyzed and compared. Focusing on the Ka-band and Ku-band σ^0 fall-off properties with incidence angles, these simultaneous measurements are shown to more precisely document differing ocean scattering characteristics for both microwave frequencies. Sensitivity with wind speed and SWH is further reported using global comparisons with numerical estimates.

Considering an extended PO approach, the interpretation of the differing sensitivity between Ku- and Ka-band near-nadir measurements is discussed. As further related to the well-known Cox and Munk optical measurements, the combined bifrequency measurements are shown to possibly efficiently separate long- and short-scale roughness elements. As presented, these combined high-frequency measurements can further help to infer total sea surface mean squared slope and to more precisely measure the influence of small-scale roughness elements. As reported, differing sensitivity is significantly obtained beyond 7 m/s. This is likely explained by the increased occurrence of steep short surface roughness scales, possibly exhibiting high curvature near their crests but also enhancing the generation surface roughness disturbances generated by breaking waves, including parasitic capillaries.

As foreseen, GPM multifrequency measurements, including both active and passive microwave observations, may serve essential practical analysis for investigations of various aspects of the air–sea interactions and remote sensing issues.

References

[1] B. Chapron, K. Katsaros, T. Elfouhaily, and D. Vandemark, "A note on relationships between sea surface roughness and altimeter backscatter," in *Proc. Air-Water Gas Transfer*, 1995, pp. 869–878.

[2] T. Elfouhaily, D. Vandemark, J. Gourrion, and B. Chapron, "Estimation of wind stress using dual-frequency TOPEX data," *J. Geophys. Res., Oceans*, vol. 103, no. 1, pp. 25 101–25 108, Oct. 1998.

[3] J. Gourrion, D. Vandemark, S. Bailey, and B. Chapron, "Investigation of C-band altimeter cross section dependence on wind speed and sea state," *Can. J. Remote Sens.*, vol. 28, no. 3, pp. 484–489, 2002.

[4] J. Gourrion *et al.*, "A two-parameter wind speed algorithm for Ku-band altimeters," *J. Atmos. Ocean. Technol.*, vol. 19, no. 12, pp. 2030–2048, 2002.

[5] G. Chen, B. Chapron, R. Ezraty, and D. Vandemark, "A dual-frequency approach for retrieving sea surface wind speed from TOPEX altimetry," *J. Geophys. Res., Oceans*, vol. 107, no. 2, pp. 19-1–19-10, Dec. 2002.

[6] M. H. Freilich and B. A. Vanhoff, "The relationship between winds, surface roughness, and radar backscatter at low incidence angles from TRMM precipitation radar measurements," *J. Atmos. Ocean. Technol.*, vol. 20, no. 4, pp. 549–562, Apr. 2003.

[7] N. Tran, B. Chapron, and D. Vandemark, "Effect of long waves on Ku-band ocean radar backscatter at low incidence angles using TRMM and altimeter data," *IEEE Geosci. Remote Sens. Lett.*, vol. 4, no. 4, pp. 542–546, Oct. 2007.

[8] X. Chu, Y. He, and G. Chen, "Asymmetry and anisotropy of microwave backscatter at low incidence angles," *IEEE Trans. Geosci. Remote Sens.*, vol. 50, no. 10, pp. 4014–4024, Oct. 2012.

[9] X. Chu, Y. He, and V. Y. Karaev, "Relationships between Ku-band radar backscatter and integrated wind and wave parameters at low incidence angles," *IEEE Trans. Geosci. Remote Sens.*, vol. 50, no. 11, pp. 4599–4609, Nov. 2012.

[10] E. J. Walsh *et al.*, "Measuring sea surface mean square slope with a 36-GHz scanning radar altimeter," *J. Geophys. Res., Oceans*, vol. 103, no. C6, pp. 12 587–12 601, Jun. 1998.

[11] E. Walsh *et al.*, "The southern ocean waves experiment. Part III: Sea surface slope statistics and near-nadir remote sensing," *J. Phys. Oceanogr.*, vol. 38, no. 3, pp. 670–685, 2008.

[12] D. Vandemark, B. Chapron, H. Feng, and A. Mouche, "Sea surface reflectivity variation with ocean temperature at Ka-band using near-nadir satellite radar data," *IEEE Geosci. Remote Sens.*, vol. 13, no. 4, pp. 510–514, Apr. 2016.

[13] C. Cox and W. Munk, "Measurement of the roughness of the sea surface from photographs of the Sun's glitter," *J. Opt. Soc. Amer.*, vol. 44, no. 11, pp. 838–850, 1954.

[14] P. A. Golubkin, B. Chapron, and V. N. Kudryavtsev, "Wind waves in the arctic seas: Envisat and Altika data analysis," *Mar. Geodesy*, vol. 38, no. 4, pp. 289–298, 2015.

[15] F. Jackson, W. Walton, D. Hines, B. Walter, and C. Peng, "Sea surface mean square slope from Ku-band backscatter data," *J. Geophys. Res., Oceans*, vol. 97, no. C7, pp. 11 411–11 427, Jul. 1992.

[16] B. Chapron, V. Kerbaol, D. Vandemark, and T. Elfouhaily, "Importance of peakedness in sea surface slope measurements and applications," *J. Geophys. Res., Oceans*, vol. 105, no. C7, pp. 17 195–17 202, Jul. 2000.

[17] O. Boisot, F. Nouguier, B. Chapron, and C.-A. Guerin, "The GO4 model in near-nadir microwave scattering from the sea surface," *IEEE Trans. Geosci. Remote Sens.*, vol. 53, no. 11, pp. 5889–5900, Nov. 2015.

[18] N. Tran and B. Chapron, "Combined wind vector and sea state impact on ocean nadir-viewing Ku- and C-band radar cross-sections," *Sensors*, vol. 6, no. 3, pp. 193–207, 2006.

[19] V. Kudryavtsev, B. Chapron, and V. Makin, "Impact of wind waves on the air–sea fluxes: A coupled model," *J. Geophys. Res., Oceans*, vol. 119, no. 2, pp. 1217–1236, Feb. 2014.

[20] B. Chapron, D. Vandemark, and T. Elfouhaily, "On the skewness of the sea slope probability distribution," in *Gas Transfer at Water Surfaces*. New York, NY, USA: Wiley, 2002, pp. 59–63.

[21] M. S. Longuet-Higgins and R. P. Cleaver, "Crest instabilities of gravity waves. Part 1. The almost-highest wave," *J. Fluid Mech.*, vol. 258, no. 1, pp. 115–129, 1994.

[22] M. Yurovskaya, V. Dulov, B. Chapron, and V. Kudryavtsev, "Directional short wind wave spectra derived from the sea surface photography," *J. Geophys. Res., Oceans*, vol. 118, no. 9, pp. 4380–4394, Sep. 2013.

[23] S. Guimbard, "Interprétation et modélisation de measures a distance de la surface marine dans le domaine micro-onde," Ph.D. dissertation, Univ. Versailles-Saint-Quentin-en-Yvelines, Versailles, France, 2010.

[24] N. Rascle, B. Chapron, A. Ponte, F. Ardhuin, and P. Klein, "Surface roughness imaging of currents shows divergence and strain in the wind direction," *J. Phys. Oceanogr.*, vol. 44, no. 8, pp. 2153–2163, 2014.